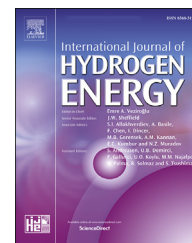




ELSEVIER

Available online at www.sciencedirect.com

ScienceDirect

journal homepage: www.elsevier.com/locate/he

Modelling and operation strategy approaches for on-site Hydrogen Refuelling Stations



Pol Cardona ^{a,*}, Ramon Costa-Castelló ^b, Vicente Roda ^d,
 Javier Carroquino ^{d,e}, Luis Valiño ^c, Carlos Ocampo-Martinez ^b,
 Maria Serra ^a

^a Institut de Robòtica i Informàtica Industrial, CSIC-UPC, Llorens i Artigas 4-6, Barcelona, 08028, Spain

^b Automatic Control Department (ESAI), Universitat Politècnica de Catalunya - BarcelonaTECH, Av. Diagonal, 647, Barcelona, 08028, Spain

^c Instituto de Carboquímica (Consejo Superior de Investigaciones Científicas), C/ de Miguel Luesma Castán, 4, Zaragoza, 50018, Spain

^d Intergia Energía Sostenible S.L., Maria de Luna 11, Nave 19, Zaragoza, 50018, Spain

^e Universidad San Jorge, Villanueva de Gállego, Zaragoza, 50830, Spain

HIGHLIGHTS

- Modelling approach of hydrogen refuelling station with on-site hydrogen production.
- Operational strategy with day-ahead scheduled grid-connected hydrogen production.
- Finite-state machine online control of a multi-tank and multi-compressor plant.
- Sensitivity analysis of hydrogen demand magnitude and frequency.
- A trade-off between demand satisfaction, profits and emissions.

ARTICLE INFO

Article history:

Received 30 April 2023

Received in revised form

11 July 2023

Accepted 15 August 2023

Available online 1 September 2023

Keywords:

Hydrogen refuelling station

Operational strategy

Modelling approach

On-site hydrogen production

Green hydrogen production

Finite-state machine

ABSTRACT

The number of Fuel Cell Electric Vehicles (FCEVs) in circulation has undergone a significant increase in recent years. This trend is foreseen to be stronger in the near future. In correlation with the FCEVs market increase, the hydrogen delivery infrastructure must be developed. With this aim, many countries have announced ambitious projects. For example, Spain has the objective of increasing the number of Hydrogen Refuelling Stations (HRS) with public access from three units in operation currently to about 150 by 2030. HRSs are complex systems with high variability in terms of layout design, size of components, operational strategy, hydrogen generation method or hydrogen generation location. This paper is focused on on-site HRS with electrolysis-based hydrogen production, which provides interesting advantages when renewable energy is utilized compared to off-site hydrogen production despite their complexity. To optimize HRS design and operation, a simulation model must be implemented. This paper describes a generic on-site HRS with electrolysis-based hydrogen production, a cascaded multi-tank storage system with multiple compressors, renewable energy sources, and multiple types of dispensing formats. A modelling approach of the layout is presented and tested with real-based parameters of an HRS currently under development, which is capable of producing 11.34 kg/h of green H₂ with irradiation at 1000 W/m². For the operation, an operational strategy is proposed. The modelled system is tested through several simulations. A sensitivity analysis of the effects

* Corresponding author.

E-mail address: pol.cardona@upc.edu (P. Cardona).

<https://doi.org/10.1016/j.ijhydene.2023.08.192>

0360-3199/© 2023 The Author(s). Published by Elsevier Ltd on behalf of Hydrogen Energy Publications LLC. This is an open access article under the CC BY-NC-ND license (<http://creativecommons.org/licenses/by-nc-nd/4.0/>).

of hydrogen demand and day-ahead hydrogen production objective on emissions, demand satisfaction and variable costs is performed. Simulation results show how the operational strategy has achieved service up to 310 FCEVs refuelling events of heavy duty and light duty FCEVs, bringing the total H₂ sold up to almost 7200 H₂kg in one month of winter. Additionally, considering variable costs of the energy from the utility grid, the model shows a profit in the range of 21–50 k€ for a daily demand of 60 H₂kg/day and 100 H₂kg/day, respectively. In terms of emissions, a year simulation with 60 H₂kg/day of demand shows specific emissions in the production of H₂ in Spain of 6.26 kgCO₂eq/H₂kg, which represents a greenhouse gas emission intensity of 52.26 gCO₂eq/H₂MJ.

© 2023 The Author(s). Published by Elsevier Ltd on behalf of Hydrogen Energy Publications LLC. This is an open access article under the CC BY-NC-ND license (<http://creativecommons.org/licenses/by-nc-nd/4.0/>).

1. Introduction

H₂ is a convenient way of storing renewable energy surplus in such a way that it can be released at a different place or time in a controlled manner, and because of that, we say that H₂ is an energy vector [1]. In particular, H₂ can be used in transportation, given its relatively high volumetric energy density when stored at high pressures.

Fuel Cell Electric Vehicles (FCEVs) use H₂ as their fuel. These types of vehicles have experienced a worldwide increase in the number of units in circulation during the last few years [2]. According to Ref. [3], almost 2500 new FCEV registrations were added in the European Union during 2021, and this number has been increasing each year. For this reason, the H₂ delivery infrastructure has been developed rapidly in the last years and this trend is foreseen to be stronger in the near future with many Hydrogen Refuelling Stations (HRSs) planned for construction [4,5]. Countries such as Spain have ambitious strategic objectives in this area, such as increasing the number of publicly available HRSs in the country from three units [6] to about 150 units by 2030 to tackle the goal of incrementing from 19 FCEVs in circulation in 2021 to more than 5000 FCEVs by 2030 [7].

HRS development has experienced a positive strong trend in the last few years. In 2021, there were 685 H₂ refuelling stations in operation worldwide, with over 130 new HRSs being added each year. It is estimated that a total of 814–975 HRSs were in operation in 2022 [2,8,9].

HRSs are complex systems with very variable designs. Nowadays, there does not exist a general solution in terms of layout or component sizing. The first degree of freedom in HRS design is to decide the location of the H₂ production. H₂ can be produced on-site in the station or it can be produced off-site in a centralized H₂ production plant [10]. On-site H₂ is an attractive solution since transportation costs are eliminated, nevertheless, a higher compression work must be performed at the station compared to an off-site HRS [10]. On-site H₂ compression is needed to achieve the targeted dispensing levels of pressure defined in the SAE TIR J2601 protocol. Water electrolysis is an interesting on-site H₂ production method since only water and electricity are required. Furthermore, if the electricity is provided by a renewable energy source such as solar photovoltaic [11], wind turbine [12] or both in a stand-

alone, self-sustainable HRS as in Refs. [13,14], then a low-emission decentralized H₂ delivery infrastructure for the transport sector is possible. The H₂ potential benefits in the self-sustainability or decentralization of energy demand in our society have been also studied for residential cases as in Ref. [15]. The simulations performed in Ref. [15], which model multiple scenarios of the operation of a multi-energy residential system (solar photovoltaic, hydrogen storage, battery, thermal storage, utility grid, fuel cell and electrolyzer), show an increase in self-sustainability from 36% to more than 70% for a H₂ penetration (hydrogen energy contribution in relation to energy demand) increase from 2% to 8%.

For HRS development, a simulation tool is needed to design the layout, size the components, develop an operational strategy, and analyse performance to be aware of the profits and potential limitations of the plant. Among the many tools for hydrogen techno-economic analysis and hydrogen technology design that the National Renewable Energy Laboratory (NREL) has developed, the Hydrogen Station Capacity Evaluation tool (HySCapE) provides a capacity estimation of a HRS with customizable configuration in terms of the number of compression stages, tanks size and dispensing lines for pre-defined fueling demand and hydrogen production profile. Nevertheless, NREL indicates this tool is not intended for control strategy development [16].

Many studies in the literature model HRSs as a single compressed H₂ gas storage system (one-tank system). The main focus of these studies is on sizing, techno-economic analysis or scheduling optimization algorithms, and the station studied is often hypothetical [11,17–20]. The recent work in Ref. [21] presents a sizing methodology based on static equations for a hypothetical grid-connected photovoltaic on-site HRS in Rabat, Morocco. These sizing equations are mainly based on linear performance coefficients of the main subsystems, constant H₂ production during operating hours and the number of FCEVs in the assumed taxi fleet case. A comprehensive techno-economic analysis of 20 years of operation of the HRS shows that a higher H₂ demand brings H₂ cost lower. Specifically, the case with the lower cost result is 9.18 USD/H₂kg, which is in accordance with the literature.

Regarding articles on real HRSs, a series of recent papers report data on the actual operation of the HRS situated in the Hydrogen Research and Fueling Facility of the California State University in Los Angeles [22–24]. Specifically, the accounting

and monitoring methodology presented in Ref. [22] successfully reduces the discrepancy between the accounted H_2 produced and H_2 dispensed from 30–35% to 2–10% by detecting sources of error such as small H_2 leaks, communication losses, methodology or procedure errors, plant dynamics, and venting. Furthermore [22], provides a set of recommendations to address these issues from the design and operating perspectives of an HRS.

In [23], the operation strategy of a real HRS is presented, which focuses on maximizing H_2 production to sequentially fill the cascaded tanks based on their pressure and demand state. However, the primary emphasis in Ref. [23] lies in highlighting the impact of back-to-back refuelling events (refuelling events occurring less than 5 min apart) on the H_2 cooling requirements, temperature dynamics during refuelling, and H_2 storage levels. Additionally, the paper provides real H_2 demand statistics and formulates key performance indicators related to refuelling performance.

Regarding the study in Ref. [24], the global data spanning multiple years of operation of the aforementioned HRS in California is presented. This data provides detailed information on energy consumption and efficiencies of various HRS subsystems. Additionally [24], formulates global key performance indicators for analyzing HRS performance, demonstrating how the improved cooling capacity and higher demand have increased the HRS efficiency to 40% in 2020 compared to the 25% efficiency recorded in 2016.

During the design of an HRS, once its layout is defined (which mainly could be summarized as which are the different compression stages, storage tank capacities and their configuration), a comprehensive modelling approach should be taken which considers the operational constraints of the layout. These operational constraints limit the HRS operational strategy compared to the assumption of a one-tank system, therefore they must be considered when optimizing the operation of a specific HRS layout by improving the operational or control strategy.

In the literature, there can be found articles focused on the detailed design and modelling of specific HRS components such as compressors [25–27], or specific processes such as the refuelling of FCEV or a H_2 tank filling process [28–30]. Regarding global HRS modelling where multiple tanks or multiple compressors are considered and the operation of the station is simulated with an online operational strategy, only a few articles as [31] can be found. More specifically [31], studies the effect of renewable energy sources dynamics and the different proposed control strategies for a hypothetical stand-alone wind turbine and solar photovoltaic HRS. The recently published article [32] is the most similar paper to the one presented in this paper. It develops a comprehensive model of a grid-connected on-site electrolysis-based HRS with off-site steam-methane reforming H_2 production, with multiple tanks, a compressor, a photovoltaic system and one dispenser. This model is simulated in a hub configuration where different H_2 demand cases are specified and interconnection between the hubs is considered. For controlling the operation of the HRS, a rule-based strategy is formulated in which the lowest pressure tank is always above a minimum value since steam-reforming H_2 input is assumed as available and presumably of high generation capacity. Multiple

simulations of the model are executed with economic and emissions results presented.

In this paper, a generic layout of an on-site electrolysis-based HRSs with a grid-connected photovoltaic system and an energy storage system capable of dispensing H_2 for three different types of clients is presented. Moreover, a general modelling approach of the main components is described and tested through simulation, with the parameters of a specific real HRS that is currently under development in Spain. An operational strategy for the HRS is proposed in which a finite-state machine controls the compressors and the on-site distribution of H_2 and a day-ahead predictive algorithm determines the grid-connected H_2 schedule of the current day. The model and operational strategy are tested through several simulation scenarios which provide a sensitivity analysis in terms of H_2 demand and other parameters. Emissions, variable costs and demand satisfaction results are presented for the stated simulation scenarios.

2. A generic HRS layout

This section presents a generic HRS layout which is shown in the scheme in Fig. 1. This scheme shows electrical power paths in orange arrows and H_2 flow rate paths in blue arrows. The sense of the arrows show in which direction the electrical power or H_2 flow rate is allowed.

Explaining Fig. 1 from the left to the right, first, a grid of e ; inter-connected electrolyzers (EL) generate H_2 as a result of a water electrolysis process, which consists of using electricity to split water molecules into H_2 and oxygen molecules. Each electrolyzer can operate in one out of two production modes: green mode and grid-connected mode. In green mode, the electrolyzer consumes electrical power from a concentrated solar cell in which the proton-exchange membrane electrolyzer is embedded. This solar cell is fed with direct-beam irradiance, G_b . The electrolyzer and solar cell are coupled with a proprietary technology that improves solar-to- H_2 conversion. On the other hand, when operating in grid-connected mode, the electrolyzer consumes electrical power from a standard grid connection point, bypassing the aforementioned solar cell.

Next to the grid of electrolyzers (EL) is a gasometer (G_1), the first and lowest pressure and mass H_2 storage stage of the HRS. The gasometer is a pressostatic gas holder that maintains a constant low pressure for the H_2 output. Its purpose is to serve as a buffer element between the electrolyzers output and compressor C_1 . It is essential to have such a storage element to unify all the H_2 produced by the electrolyzers and prevent C_1 outflow rate fluctuations from damaging any of the electrolyzer units. Furthermore, it is necessary to size the gasometer appropriately to ensure that it provides the inlet pressure recommended by the C_1 manufacturer for the best compression efficiency.

Between G_1 and C_1 , there is the purifier P1. Purification is required since compressors may leak oil [33], as well as the piping or valves [34] or the H_2 source [10]. Acceptable H_2 purities should be above 99.97% [35].

At the output of P_1 , there is compressor C_1 , which is responsible for boosting H_2 pressure from an inlet steady low-

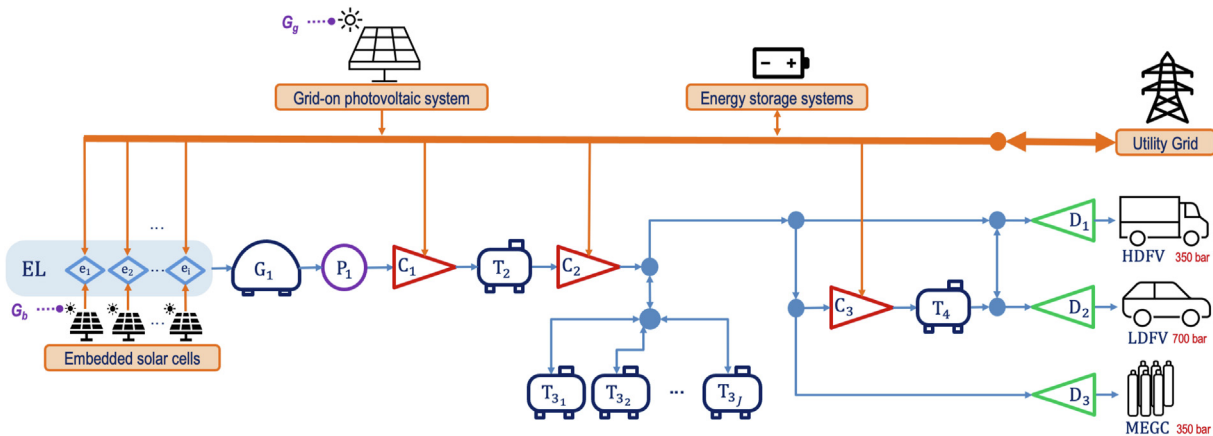


Fig. 1 – HRS plant scheme.

pressure value to an outlet mid-range level of H_2 pressure in T_2 . The purpose of using multiple tanks in series is to be able to use smaller compressors.

Compressor C_2 is responsible for filling a high-pressure cascaded subsystem consisting of j tanks (T_{3j}). T_{3j} is designed to be filled and emptied sequentially, providing better performance in direct tank-to-tank expansion processes by taking advantage of the high pressure of non-emptied tanks [36]. Compared to a one-tank solution, a 12% reduction in compression energy demand and a 19% reduction in high-pressure H_2 storage capacity is required in the three-tank cascaded system presented in Ref. [37]. Furthermore, 6% energy savings can be achieved with a three-tank cascaded system compared to a one-tank solution, as reported in Ref. [38].

Fig. 2 illustrates that C_2 consists of a two-stage compression process, which includes two compressors, namely C_{21} and C_{22} , with a buffer tank (TB) located in between.

In Fig. 1, the node that connects the C_2 output and the input/output of T_{3j} , H_2 gas paths leads to two dispenser stages and one compression stage. The two dispenser stages that are directly connected to either C_2 output or T_{3j} are designed to refuel Heavy Duty Fuel cell Vehicles (HDFVs) through dispenser D_1 and Multiple Element Gas Containers (MEGCs) through dispenser D_3 , both with an A35 rating according to the protocol SAE TIRJ260 [37]. Besides, the H_2 stored in T_{3j} must be compressed further through C_3 to a higher than 700 bar

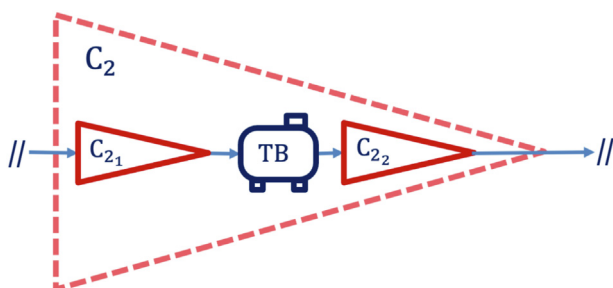


Fig. 2 – C_2 detailed scheme.

pressure to be able to refuel Light Duty Fuel cell Vehicles (LDFVs) through D_2 with an A70 rating [37]. For this reason, T_4 is placed at the output of C_3 . This layout brings considerable flexibility since a hybrid of the two primary layouts with gaseous storage is considered [10]: cascade refuelling and direct refuelling with the use of a hydrogen compressor.

The renewable HRS layout depicted in Fig. 1 is designed to be connected to the power grid, which means that it can draw power from two different sources: renewable energy sources and the utility grid. Additionally, the HRS is equipped with electrical energy storage systems that allow energy to be stored and used afterwards as needed.

In terms of design, the energy storage system is considered due to its potential in reducing the load peaks in the utility grid. Including an energy storage system is advantageous because the electrical energy provider of the HRS will likely have an upper power constraint based on the power lines at the location or contract with the HRS operator. In addition, the cost increases with higher power lines or contracts, even if the feasibility of a high power connection point available at the HRS location is assumed. From a control standpoint, the addition of an energy storage system provides an additional degree of freedom that may enhance the overall optimization of the HRS performance.

In Fig. 1, a grid-on photovoltaic system is shown, whose output depends mainly on global irradiance, G_g .

Disturbances are presented in purple in Fig. 1. These are irradiances G_b and G_g .

In Fig. 1, the power flow to the utility grid is bidirectional, hence the HRS can either consume or inject power to the utility grid, buying or selling energy, respectively.

3. Simulation model

This section introduces the models of the main components of the HRS needed to develop a Simulation-Oriented Model (SOM) of the HRS. In this case, MATLAB/Simulink[®] has been employed as the simulation platform.

3.1. Electrolyzers

The grid of e_i inter-connected electrolyzers has been modelled as an aggregate electrolyzer since the manufacturer provides expected performance data for the overall grid.

The model of the unified electrolyzer dynamics has been straightforward since enough information from the manufacturer has been provided. Then, we know with suitable accuracy the two most relevant features of the on-site HRS performance: the H_2 production capacity and the amount of energy needed.

The electrolyzer production modes are green mode and grid-connected mode, which are described as follows:

- Green mode: a linear relationship between G_b and the green H_2 outflow rate is provided by the manufacturer. This irradiance-to-flow relationship factor is β_{EL_IR2F} in $\frac{kg/h}{1000W/m^2}$.
- Grid-connected mode: one out of five discrete levels of constant H_2 production outflow can be selected. Each level h has a constant output flow rate, e_{F_h} . The electrolyzers manufacturer provides the power consumption data for each level h (from 1 to 5), e_{P_h} .

Hence, the electrolyzer modelling problem has been divided into two models, one models the H_2 flow rate, EL_{flow} , in kg/h, and the other the power consumption for H_2 production, EL_{power} , in kW. The inputs of the model are the irradiance G_b in W/m^2 (which acts as a disturbance) and the operating mode selector, EL_{lvl} (which acts as a control variable). Since the electrolyzers production modes are logically exclusive, only one mode can be selected at once. The model should be described as a piecewise affine function. In addition, the electrolyzers emergency stop must be considered in the model. For this reason, whenever the binary control variable EL_{STOP} is true, EL_{flow} and EL_{power} are set to 0, independently of the value of EL_{lvl} .

EL_{flow} and EL_{power} are described in Equation (1).

$$EL_{flow}(t) = \begin{cases} 0, & \text{if } EL_{STOP}(t) = 1 \\ \beta_{EL_IR2F} \frac{G_b(t)}{1000}, & \text{if } EL_{STOP}(t) = 0 \text{ and } EL_{lvl}(t) = 0 \\ e_{F_h}, & \text{if } EL_{STOP}(t) = 0 \text{ and } EL_{lvl}(t) \forall h \in [1, 5], \end{cases} \quad (1a)$$

$$EL_{power}(t) = \begin{cases} e_{P_h}, & \text{if } EL_{STOP}(t) = 0 \text{ and } EL_{lvl}(t) \forall h \in [1, 5] \\ 0, & \text{otherwise} \end{cases} \quad (1b)$$

The model for the electrolyzer has two inputs and two outputs. The inputs are EL_{lvl} , which is an integer variable ranging from 0 to 5, and the binary variable EL_{STOP} . The two outputs are EL_{flow} in kg/h and EL_{power} in kW.

3.2. Storage tanks

Compressed H_2 storage tanks have been all modelled under the ideal gas equation with the compressibility correction factor Z . This assumption is presented in Equation (2), whose output is the H_2 amount of pressure in bars for a constant volume tank in which compression has been assumed isothermic. Hence, the

general internal tank pressure is defined in Equation (2), where R is the ideal gas constant ($83.1447 \text{ L mbar (K mol)}^{-1}$), T_H is the H_2 temperature in K, M is the H_2 molar mass equal to 2.02 g mol^{-1} , V is the tank volume in m^3 , \dot{m}_{in} and \dot{m}_{out} are, respectively, the tank H_2 inflow and outflow rates in $kg h^{-1}$, $m(0)$ is the tank initial H_2 mass in kg, and $Z(t)$ is the compressibility factor which depends on the ideal pressure $P_0(t)$ (Equation (2)) without $Z(t)$ correction) and the H_2 temperature $T_{H(t)}$ in K [39].

$$P(t) = \frac{R T_H(t)}{M V 3600} \left[\int_0^t (\dot{m}_{in}(t) - \dot{m}_{out}(t)) dt + m(0) \right] \frac{Z(t)}{1000} \quad (2)$$

Since the temperature effects are not considered, all tanks stored H_2 temperature is assumed to be equal to ambient temperature.

The function $Z(t)$ has been obtained by digitalizing the graph provided by Refs. [39,40]. For digitalizing, it is appreciated [41] for providing such a complete and free tool with many options and high accuracy.

It has been chosen to digitalize independently the 200 K, 250 K, and 300 K cases of the H_2 compressibility factor [39,40] and map them to a lookup table.

For the case T_3 , Equation (2) must be slightly modified due to these tanks only presenting one shared input/output H_2 path, as seen in Fig. 1. Hence, the term $\dot{m}_{in}(t) - \dot{m}_{out}(t)$ in Equation (2) is substituted by $\dot{m}_{inOut}(t)$, which is a signed flow, where a positive sign means H_2 mass is introduced to the tank while a negative sign means H_2 mass is leaving the tank.

To summarize, the set of models of the tanks have three inputs: $\dot{m}_{in}(t)$ and $\dot{m}_{out}(t)$ in $kg h^{-1}$, and ambient temperature in K. Two inputs are required for T_3 , which are $\dot{m}_{inOut}(t)$ in $kg h^{-1}$ and ambient temperature in K. All tanks model output is $P(t)$ in bar.

3.3. Compressors

H_2 compressors are responsible for boosting the inlet gas pressure to a higher outlet amount of pressure. Two output variables have been modelled for this process: H_2 flow rate and power consumption. Temperature dynamics are not considered, hence perfect cooling is assumed.

When modelling a compressor, the general assumption is to consider compression an isentropic or a polytropic process. Isentropic compression work of a compressor is considered in Refs. [42,43]. Polytropic compression work of a compressor is considered in Refs. [38,42–45].

Compressor manufacturers provide some dynamics and performance data of each compressor in a graphical or tabulated format. For this reason, the power and flow rate model proposed by Ref. [43] has been adopted, which adds seven empirical parameters to the isentropic compression assumption that fits the model to manufacturer empirical data.

The model of the volumetric gas flow rate, \dot{V}_{comp} , in Nm^3s^{-1} of a compressor is described in Equation (3), where N is the compressor speed in min^{-1} , V_{disp} is the displacement of the compressor in m^3 , and η_v is the volumetric efficiency defined in Equation (4) [43].

$$\dot{V}_{\text{comp}}(t) = 60N(t)V_{\text{disp}}\eta_v(t) \quad (3)$$

$$\eta_v(t) = b_1 + b_2 \left[\left(\frac{P_{\text{outlet}}(t)}{P_{\text{inlet}}(t)(1-dp)} \right)^{1/k} \right] \quad (4)$$

$$C_{\text{power}}(t) = P_{\text{inlet}}(t)\dot{V}_{\text{comp}}(t) a_1 \left[\left(\frac{P_{\text{outlet}}(t)}{P_{\text{inlet}}(t)} \right)^{a_2 + \frac{k-1}{k}} + \frac{a_3}{P_{\text{outlet}}(t)} \right] + W_{\text{loss}} \quad (5)$$

In Equation (4), P_{inlet} and P_{outlet} are the inlet and outlet pressures in Pa, respectively, k is the heat capacity ratio assumed constant, b_1 and b_2 are empirical parameters that must be obtained with empirical data fitting. Moreover, dp represents the relative pressure drop at the inlet of the compressor, which is also an empirical parameter to be fitted.

The power of the compressor at the shaft, C_{power} , is defined in Equation (5) [43], where a_1 , a_2 , and a_3 are empirical parameters that must be obtained with empirical data fitting, and W_{loss} is a constant power loss in W, which is also an empirical parameter to be fitted.

The process for extracting the set of seven empirical parameters for each compressor of Fig. 1 has been the next:

1. If possible, extract N and V_{disp} from the provided datasheets. If not, assume values similar to other comparable compressors datasheets.
2. If possible, digitalize the flow and power graphs provided by the manufacturer and take the inlet and outlet pressure conditions. If not, extrapolate from another compressor that provides a similar outflow range.
3. Fit the flow model and power model.
4. Simulate each model, flow and power, with the fitted parameters at the conditions of the manufacturer and compare results with the provided or assumed graphs of step 2. If the results are not acceptable, change the assumed parameters, limits, or starting values in the fitting algorithm and go to step 3.

When digitalizing both graphs, power consumption in terms of pressure and outflow rate in terms of pressure, the two sets of data must have the same x-axis query values (pressure). This is because the power consumption depends on the outflow rate and pressure, hence the outflow fed to the power consumption in Equation (5) must be for the same pressure values that the power is being computed. For this [41], provides the option to fix an x-axis step in extracting the values from the graph.

All H_2 compressors models have a binary control signal, C_{iEN} , that turns on or off the compressor if the signal is set to 1 or zero, respectively. When C_{iEN} is set to 0, the power consumption and the flow rate through the compressors are null. When C_{iEN} is set to 1, the power consumption and flow rate is the one described in Equation (5) and Equation (3), respectively. Hence, each compressor model has three inputs: inlet and outlet pressure in Pa and the enable signal. The compressors model outputs are the volumetric flow rate in Nm^3s^{-1} and the power consumption in W.

3.4. Solar photovoltaic system

The grid-on photovoltaic system shown in Fig. 1 transforms solar irradiance energy into electrical energy. The grid of photovoltaic panels has been modelled as an aggregate solar panel and it is assumed it operates at the maximum power point. For this reason, the model proposed in Ref. [46], which is based on [47], has been adopted. The model proposed in Ref. [47] is attractive since it provides an easy closed-form estimation of the entire current-voltage curve, the fill factor, and the maximum power point [48]. The paper done in Ref. [46] provides the adaptation of the equations presented in Ref. [47] to conditions different to Standard Test Conditions (STC). This method is called Approximate Maximum Power Point (AMPP). Such a method uses the short-circuit current and open circuit voltage at STC to approximate the solar panel current and voltage of the maximum power point at the operating panel conditions. Moreover, this model only requires parameters commonly found in solar panels datasheets, hence it is a reasonable first approach since parameters provided by the manufacturer are used and maximum power point is estimated. The AMPP method shows less than an 8% error compared to empirical data in tests done in Ref. [46].

Before applying AMPP, the solar cell temperature at operating conditions, T_{OpC} , is required which is not provided in Refs. [46,47]. The cell temperature estimation considered in this paper is the one shown in Ref. [45] with the back surface temperature of the module assumed equal to the ambient temperature. Hence, T_{OpC} is a function of the ambient temperature, T_a , and global irradiance, G_g . This function is defined in Equation (6), where NMOT refers to the Nominal Module Operating Temperature in $^{\circ}\text{C}$, G_{NMOT} is the global irradiance under NMOT in W/m^2 , and T_{aNMOT} is the ambient temperature in $^{\circ}\text{C}$ at NMOT conditions.

$$T_{\text{OpC}}(t) = T_a(t) + \frac{G_g(t)}{G_{\text{NMOT}}} (\text{NMOT} - T_{\text{aNMOT}}) \quad (6)$$

The set of AMPP equations considered in this paper can be found in Ref. [46]. This model is fed with two inputs: the global irradiance, G_g , in W/m^2 and ambient temperature, T_a , in $^{\circ}\text{C}$. The only output of the model is the maximum power point of the overall photovoltaic system, P_{mp} , in kW.

3.5. Hydrogen demand

The H_2 demand in this study is represented by HDFVs, LDFVs, and MEGCs. HDFVs and LDFVs are modelled as H_2 tanks that are always connected to their respective dispensers, set with two additional signals. One binary signal acts as a disturbance and is set to 1 to emulate the respective vehicle arrival, $HDFV_{\text{ar}}$ or $LDFV_{\text{ar}}$. This signal set to 1 means that a FCEV has arrived at a dispenser and needs to be serviced, hence corresponding refuelling processes must be initiated, if feasible. The second binary signal required is for emulating the vehicle departure from the dispenser with $HDFV_{\text{dp}}$ or $LDFV_{\text{dp}}$. This departure signal set to 1 means that no vehicle is waiting for service, hence D_1 and D_2 are deactivated and other processes can be prioritized. This departure signal also resets the accumulated mass of the tanks to a

certain level, which is the next client-assumed initial H_2 stored mass. $HDFV_{dp}$ and $LDFV_{dp}$ are generated from the control unit.

It has been assumed that HDFVs and LDFVs clients always seek refuelling completion. For this reason, it has been assumed as refuelling completion thresholds that HDFVs leave the station when a pressure level of 350 bar is achieved and LDFVs leave the station when a pressure level of 700 bar is achieved. In addition, the control unit emulates a vehicle departure when continuing the refuelling process is not feasible which means HDFVs and LDFVs are not modelled as waiting clients. If continuing a refuelling procedure is not feasible, it is left uncompleted by resetting the respective vehicle tank with $HDFV_{dp}$ or $LDFV_{dp}$ signal set to 1.

Arrival $HDFV_{ar}$ and $LDFV_{ar}$ signals can be externally generated as time-dependent profiles.

MEGCs, on the other hand, are modelled internally as a controlled service, and thus the control unit decides when H_2 is sent to the MEGCs to be sold. It is assumed that when MEGCs are full, they are immediately replaced with empty units, thus only the total derived H_2 mass has been modelled by integrating its respective dispenser flow over time.

3.6. Other components

The energy storage system has been modelled as a linear electrical energy storage system. Consequently, the State of Charge (SoC) in % of the system is defined in Equation (7), where C is the system capacity in kWh, $P_{ESS}(t)$ is the signed power applied to the system with positive and negative signs meaning the system is being charged or discharged, respectively. In addition, $SoC(0)$ is the initial SoC. Hence, this linear model takes $P_{ESS}(t)$ in kW as the only input and SoC in % as the only output.

$$SoC_{ESS}(t) = \frac{100}{3600C} \int_0^t P_{ESS}(t) dt + SoC(0) \quad (7)$$

Dispensers monitor and control the hydrogen flow rate during the refuelling procedure [10]. In this paper, dispensers are modelled as ideal on/off controlled valves. Hence, the H_2 flow rate output of the dispenser in kg/h, \dot{m}_{disp} , model is described in Equation (8).

$$\dot{m}_{disp} = \begin{cases} \dot{m}_{in}, & \text{if } D_{EN}(t) = 1 \\ 0, & \text{otherwise} \end{cases} \quad (8)$$

In Equation (8), D_{EN} is the respective dispenser binary enable control signal. Hence, each dispenser model has two inputs: H_2 flow rate going into the dispenser, \dot{m}_{in} , in kg/h, and D_{EN} . Each dispenser model output is \dot{m}_{disp} in kg/h.

The pressostatic gasometer has been assumed ideal, hence its pressure is constant at a given value for a stored H_2 mass range specified by the manufacturer.

The gasometer model has two inputs, the inlet and outlet H_2 mass flow rate \dot{m}_{in} and \dot{m}_{out} , respectively, in kg/s. These two flow rates are integrated to monitor the stored H_2 mass. The outputs of the gasometer model are the constant pressure in bar and the H_2 mass stored.

3.7. General model assumptions

The main list of assumptions of the presented model are:

- H_2 is considered an ideal gas with compressibility factor correction implemented using a 2-D lookup table.
- Temperature, pressure or H_2 losses are not considered. H_2 temperature is considered equal to ambient temperature.
- Gas compression is isothermal (ideal H_2 coolers are implicitly considered).
- Ideal power converters for the photovoltaic system and the energy storage system are considered, they do not add power dynamics or power losses.
- Direct expansion flow rate (i.e., tank to vehicle or tank to MEGC) is considered constant at 216 kg/h (0.67 Nm³/s) for dispensers intended to refuel HDFVs, 108 kg/h (0.34 Nm³/s) for dispensers of LDFVs, and 180 kg/h (0.56 Nm³/s) for dispensers of MEGCs.
- FCEV refuelling completion has been assessed in terms of a hydrogen pressure threshold: 350 bar for HDFV and 700 bar for LDFV.
- MEGCs are considered as an infinite volume tank, hence their replacement when full is implicitly assumed. Nevertheless, their pressure is considered constant at 175 bar.
- On/Off controlled valves are assumed ideal, which means no delay is considered.
- Purification is assumed ideal, no pressure drops or flow rate dynamics are considered.

4. Operational strategy

The dynamic behaviour of the HRS model introduced in this paper cannot be tested without an operational strategy implemented through a control strategy. This section firstly describes the set of operational constraints of the HRS and secondly, introduces the operational strategy that determines all the HRS model control actions. The operational strategy consists of a finite-state machine and a day-ahead predictive algorithm.

4.1. Operational constraints

In order to set any operational strategy, the operational constraints of the plant must be accounted for. These constraints determine how the different components are allowed to be operated individually as well as how they are allowed to interact with each other. In this subsection, the set of operational constraints is introduced.

The scheme in Fig. 1 shows that all T_3 are connected in parallel to the same bidirectional path. It means that it is not possible to fill one tank while emptying any of the others. Moreover, emptying all T_3 tanks at the same time is not possible. Finally, when emptying any of the T_3 tanks, it is necessary to turn C_2 off.

Thus, for filling T_4 up, only one T_3 must be selected to feed C_3 while C_2 is turned off.

HDFV and MEGC simultaneous service is not permitted. In addition, during any of these two services, C_3 must be turned off.

The output of C_2 , any of T_3 , or T_4 cannot be shared with D_1 and D_2 simultaneously. It means simultaneous refuelling of HDFV and LDFV from the same tank source is not permitted.

In the case of the energy storage system, it can be independently controlled to supply energy to the microgrid (discharging) or act as a load (charging). Nevertheless, the power on either mode must be contained in a certain power range.

4.2. Operational state machine

The operational strategy that decides which compressors and dispensers are enabled and which path of H_2 is selected has been formulated as a Rule-Based Control (RBC) implemented into a finite-state machine. Such a machine has been developed in the Stateflow environment of MATLAB/Simulink®. The following paragraphs describe the main logic of operation considered in the finite-state machine.

Regarding T_4 , it is filled up with the highest priority since it can achieve the highest pressure necessary to refuel HDFVs or LDFVs of any level of charge. T_4 is filled up from one of the tanks T_3 . The T_3 selected is the one with an amount of pressure nearest but greater to the C_3 best inlet pressure recommended by the manufacturer. If there is not a T_3 above that amount of pressure, tanks T_3 are filled and then T_4 .

The cascaded refuelling process is a tank-to-tank process where the H_2 flow rate stops when the pressure in the source tank (T_3) is equal to the output tank (HDFV or LDFV). Therefore, the finite-state machine does not consider a T_3 as available if its pressure is equal to or less than the target HDFV or LDFV amount of pressure at any time during refuelling.

The order of filling the cascaded subsystem of T_3 is from the tank with the highest pressure to the one with the lowest. Once a tank is selected, it is not changed until it is filled up. This logic is similar to that of [30] with the difference that they consider different maximum pressure levels of the cascaded tanks.

In the case of HDFV or LDFV arrival, all active filling processes described before are stopped to start the corresponding refuelling procedure by setting either D_{1EN} or D_{2EN} to 1 (enabled).

The order of priority for refuelling HDFVs and LDFVs is the same in both cases. If possible, the T_3 with the lowest pressure above the vehicle pressure is selected to refuel the vehicle. In case of pressure equilibrium and the vehicle not being full, the next T_3 with the lowest pressure above the vehicle pressure is selected and so on. If none of the T_3 has a pressure higher than vehicle pressure but T_4 pressure is, T_4 is emptied until pressure equilibrium or refuelling completion. If refuelling is still not completed, the vehicle is refuelled with direct refuelling through C_2 if T_2 is in a certain range of pressure. In the case of LDFVs, C_2 stops refuelling if the vehicle pressure is above the maximum outlet C_2 amount of pressure. If refuelling is still not complete, it is left unfinished, and the respective vehicle departure is emulated (resetting either the HDFV or LDFV tank with the $HDFV_{dp}$ or $LDFV_{dp}$ signal set to 1). After refuelling completion or refuelling failure, the respective dispenser enabling control signal, D_{1EN} or D_{2EN} , is disabled (set to 0).

In the case of MEGCs service, only filling them up through C_2 is considered. MEGCs are only filled when all T_3 and T_4 are full and T_2 is in a certain range of pressure.

Concerning C_1 , it is turned on whenever the pressure of T_2 is less than a high-pressure threshold and the mass at the gasometer is greater or equal to a high-mass threshold. C_1 is turned off when T_2 pressure is above or equal to a high-pressure threshold or the mass at the gasometer is less than or equal to a low-mass threshold.

The operational strategy simplified flow chart of the main filling and refuelling procedures is shown as Supplementary Material.

The control of the energy storage system is entirely based on the current power balance of the grid-connected microgrid, P_{MG} , and the SoC_{ESS} . The power balance of the grid-connected microgrid is defined in Equation (9) with all power units in kW.

$$P_{MG}(t) = -EL_{power}(t) - C_{1power}(t) - C_{2power}(t) - C_{2power}(t) - C_{3power}(t) + P_{mp}(t), \quad (9)$$

The energy storage system is charged during a surplus of more than 10 kW in P_{MG} with P_{ESS} matching the surplus of power until the maximum charging power specification. Furthermore, charging is initiated if SoC_{ESS} is less than 90% until the surplus of 10 kW no longer exists or the SoC_{ESS} is greater or equal to 100%.

The energy storage system is discharged whenever P_{MG} is less than -10 kW with P_{ESS} matching the deficit of power until the maximum discharging power specification. Moreover, discharge is initiated if SoC_{ESS} is greater than 40% until the electric load of -10 kW no longer exists or the SoC_{ESS} is less or equal to 20%.

If charging or discharging is not feasible, the energy storage system is in a standby state with P_{ESS} set to 0 kW.

The HRS model provides the electric power being consumed or injected into the utility grid, P_{GRID} , which is defined in Equation (10)

$$P_{GRID}(t) = P_{ESS}(t) + P_{MG}(t). \quad (10)$$

4.3. Day-ahead predictive algorithm

Here, it is decided to control the generation of H_2 from the utility grid independently as it is a crucial decision in satisfying demand. Therefore, an adapted version of the deterministic day-ahead scheduling algorithm with prediction data reported in Ref. [49] is adopted. This algorithm schedules the future hours in which the electrolyzers will produce H_2 in grid-connected mode. This scheduling covers a 24-h period and it is updated daily at 00:00 a.m., providing 24 hourly values of $EL_{|v|}$ for the next day.

The algorithm takes four inputs each day at 00:00 a.m.:

- The sum of H_2 mass of all T_3 and T_4 .
- The next 24 h of hourly G_b profile prediction data, p_{G_b} .
- The next 24 h of hourly grid energy prices, e_p , profile prediction data, p_{e_p} .
- The next 24 h total HDFV and LDFV H_2 mass demand prediction.

The main logic of the algorithm is to calculate the next-day potential deficit of green H_2 production in terms of the estimated demand, taking into account the state of the plant at 00:00 a.m. This deficit is written as

$$\Gamma(t) = \max\{\gamma(t), 0\}, \quad (11)$$

where $\Gamma(t)$ is the next-day H_2 mass deficit and $\gamma(t)$ refers to the H_2 mass balance defined as

$$\gamma(t) = Y(t) + \delta(t) - \sum_{i=1}^{24} \left[p_{G_b}(i) \frac{\beta_{EL_IR2F}}{1000} \right] - \Phi, \quad (12)$$

where $Y(t)$ is the scalar prediction of total HDFV and LDFV mass demand for the day, Φ is the total daily scheduled mass for grid-connected H_2 production mode, p_{G_b} refers to the vector of 24 h of predicted hourly direct-beam irradiance, G_b , profile for the day, and $\delta(t)$ is the H_2 mass regulation error of the T_3 and T_4 tanks, defined as

$$\delta(t) = \lambda - \left[x_4(t) + \sum_{i=1}^4 x_{3_i}(t) \right]. \quad (13)$$

This regulation error adjusts the overall grid-connected production objective of the day in terms of how T_3 and T_4 tanks stored H_2 mass states, $x_{3_{1..4}}$ and x_4 , are at 00:00 a.m. each day.

If the next-day deficit of H_2 is positive ($\Gamma > 0$), the equivalent minimum necessary hours of the electrolyzers at constant maximum grid-connected mode production ($EL_{iv1} = 5$ in Equation ()) is used to cover the deficit. The algorithm selects the appropriate hours to maximize EL_{iv1} based on the lowest possible irradiance and grid energy price hours, which is reasonable for maximizing green H_2 and minimizing economic cost. To account for multiple criteria, normalization and weighting are applied. Two weights, whose sum equals 1, are then multiplied independently to each normalized prediction vector, $p_{G_b}^*$ and $p_{e_p}^*$. Additionally, to produce H_2 early in the day, the first 8 h of $p_{e_p}^*$ are reduced by 20%. Then, $p_{G_b}^*$ and $p_{e_p}^*$ are hourly summed up to obtain an hourly vector valuation of the multiple criteria, p_v .

The algorithm iteratively assigns EL_{iv1} at its maximum value as many hours as necessary to cover a $\Gamma > 0$, selecting the hours based on p_v , starting from the lowest to the highest value. At each iteration, the selected hour at which EL_{iv1} has been set to 5 is updated, the same hour value of p_{G_b} is set to 0, and Φ in Equation (12) is updated based on the new electrolyzers grid-connected mode production schedule and the respective electrolyzer grid-connected production level in Equation (). Then, $\gamma(t)$ in Equation (12) is recalculated, and the loop is executed again for the next lowest value in p_v . The loop is concluded once $\gamma(t)$ in Equation (12) gives a negative result, indicating that the initial deficit has been covered with Φ in Equation (12).

5. Simulation results

In this section, an analysis is conducted on the results of multiple simulation scenarios using the HRS model developed in this paper. The simulations are based on a specific set of parameters corresponding to the case of study concerning the HRS of the TRE2103000 project, which is planned to be constructed in Zaragoza, Spain.

5.1. Case of study parameters

The parameters of the components of the HRS presented in this section are provided by the respective manufacturers. In the cases in which parameters are not available, an assumption of the values is introduced.

Regarding the electrolyzers configuration, 22 inter-connected electrolyzers are considered. The provided irradiance-to-flow relationship factor of the electrolyzers in green H_2 production mode, β_{EL_IR2F} , is $11.34 \frac{\text{kg/h}}{1000\text{W/m}^2}$ and the discrete grid-connected levels are described in Table 1.

Tanks volume and maximum pressures, P_{\max} , are resumed in Table 2. As can be seen, the cascaded subsystem consists of four tanks.

For all refuelling services, the assumed volume of the HDFV tank is set to 1.955 m^3 , while the assumed volume of the LDFV tank is set to 0.181 m^3 .

The gasometer is designed to store a maximum of 12 kg of H_2 for a steady output pressure of 0.035 bar.

Compressors flow range specification and conditions are listed in Table 3. They are values provided by manufacturers.

In Table 4, the speed, N , and the displacement volume, V_{disp} of each compressor are defined. In addition, assumed values are marked with dark grey cells.

The speed of C_1 may be a point of contention, as it is not feasible to achieve it with a synchronous motor in Spain due to the 50 Hz utility grid. However, it is the only nominal specified parameter for the flow rate and power data presented in Table 3 by the manufacturer.

The manufacturer of C_1 does not provide flow rate or power graphs. To address this issue, it is used a linear extrapolation of C_{2_1} data based on the nominal specifications provided in Table 3. This extrapolation enables the application of the parameter fitting procedure described in Section 3.3.

Table 5 provides the parameters obtained by data fitting for each compressor. These parameters are needed for Equation (3) and Equation (5).

Due to the lack of information on the buffer tank TB in between C_{2_1} and C_{2_2} , it has been assumed that C_{2_1} and C_{2_2} flow rates are equal and TB pressure remains constant. Therefore, only C_{2_1} flow rate model has been considered. C_{2_1} and C_{2_2} power consumptions are modelled as a global one-compression stage, $C_{2_{os}}$. To estimate the empirical parameters of $C_{2_{os}}$, C_{2_2} power consumption has been linearly extrapolated to C_{2_1} flow rate range and added to respective C_{2_1} power consumption values. The fitted parameters obtained for $C_{2_{os}}$ power model are provided in Table 6.

Table 1 – Performance data of the levels of grid-connected mode production of the grid of electrolyzers: H_2 outflow rate and power consumption.

Grid-connected level	H_2 production (kg/h)	Power consumption (kW)
1	1.99	83.64
2	3.74	174.87
3	7.48	380.16
4	10.76	590.20
5	13.12	789.47

Table 2 – H₂ storage tanks specifications.

Tank	Volume (m ³)	P _{max} (bar)	P _{max} (MPa)
T ₂	50	40	4
T _{3,1,2,3,4}	1.12	500	50
T ₄	0.55	960	96

Table 3 – Compressors nominal specifications.

Compressor	Maximum Output		Pressure conditions (bar)	
	kg/h	Nm ³ /s	Inlet	Outlet
C ₁	11.23	0.034	0.035	40
C _{2,1}	30.29	0.093	30	185
C _{2,2}	33.08	0.102	185	500
C ₃	20.31	0.062	500	1000

Table 4 – H₂ compressors specifications, dark grey cells for assumed values.

Compressor	N (min ⁻¹)	V _{disp} (dm ³)
C ₁	1600	9.05
C _{2,1}	3000	9.05
C _{2,2}	3000	4.02
C ₃	3000	7.95

The grid-on photovoltaic system is comprised of 322 solar panels placed in series and parallel. Each solar panel has a nominal maximum power output of 545 W under STC (1000 W m⁻², spectrum AM 1.5 and cell temperature of 25 °C) or 406 W under NMOT conditions (irradiance of 800 W m⁻², spectrum AM 1.5, ambient temperature 20 °C, wind speed 1 m/s). The grid-on photovoltaic system specifications are listed in Table 8, while dispenser specifications are provided in Table 7.

The energy storage system considered is an electrochemical battery with a charging/discharging capacity of ± 200kW range.

The finite state machine considers refuelling through C₂ if T₂ is above 28 bar until 26 bar is reached or refuelling completion. In the case of LDFV refuelling, C₂ is turned off if the vehicle amount of pressure is above 500 bar since it is the maximum outlet amount of pressure of C₂.

C₁ is turned on when the gasometer is at its maximum capacity and T₂ pressure is less or equal to 30 bar. C₁ is turned off when the gasometer is under 1 kg of H₂ or T₂ pressure is equal to or greater than 32 bar, which is the maximum outlet pressure of C₁. If the gasometer and T₂ are at 12 kg and 32 bar, respectively, the electrolyzers are turned off by setting EL_{STOP} to 1, otherwise, it is 0.

Table 6 – Data-fitted parameters for the assumed compressor C_{2,os} power consumption model.

Compressor	a ₁	a ₂	a ₃	W _{loss} (W)
C _{2,os}	0.004	1.102	1	10,800

Table 7 – Dispensers specifications.

Dispenser	Maximum Output	
	kg/h	Nm ³ /s
D ₁	216	0.67
D ₂	108	0.34
D ₃	216	0.67

Regarding the day-ahead predictive algorithm, the weights applied to the normalized irradiance and energy price prediction have been 0.8 and 0.2, respectively.

5.2. Simulation scenarios

The simulation scenarios formulated in this paper aim to assess the impact of HDFV and LDFV demand on the HRS case study performance, specifically in terms of demand satisfaction, emissions, energy consumption, and profits. To study the effect of FCEV demand, two factors are considered: the time of arrival of the vehicle and the quantity of mass refuelled. To this end, it has been devised a deterministic methodology to assess the effect of the two uncertain factors in a deterministic sensitivity analysis.

Firstly, three scenarios of daily demand (60, 100, and 140 kg/day) have been established for all days of the simulation. For all demand scenarios, two LDFVs arrive each day and each of them requires 5 kg of H₂, which translates to 10 kg/day refuelled to LDFVs. For each daily demand scenario, three scenarios of intra-daily HDFV frequency (3, 5, and 8 HDFVs per day) are imposed. HDFV refuelling services are equally distributed in the 8 a.m. to 10 p.m. hours range of each day of simulation. The first LDFV always arrives between the first and second HDFV, and the second LDFV arrives between the last two HDFVs for each HDFV frequency case.

The mass refuelling objective for each HDFV is the same for each HDFV frequency case, which is the result of distributing the daily demand scenario equally, after deducting the 10 kg/day of LDFV, between the number of HDFV per day. Additionally, for each daily demand scenario, the daily demand prediction, Υ in Equation (12), has been perfect, resulting in the same value as the daily demand scenarios (60, 100, and 140 kg/day) for each respective case.

Table 5 – Data-fitted parameters of the compressors flow rate and power consumption models.

Compressor	b ₁	b ₂	dp	a ₁	a ₂	a ₃	W _{loss} (W)
C ₁	8.046 × 10 ⁻⁵	-2.214 × 10 ⁻⁷	0.091	0.097	1.034	-1.657 × 10 ⁻⁷	11.53
C _{2,1}	1.056 × 10 ⁻¹⁰	-1.234 × 10 ⁻⁵	0.091	0.004	1.1711	1.526 × 10 ⁷	4658.9
C _{2,2}	3.053 × 10 ⁻⁴	-7.569 × 10 ⁻⁵	0.091	0.0016	1.2937	-49.047	3300
C ₃	6.591 × 10 ⁻⁵	-1.473 × 10 ⁻⁵	0.091	8.02 × 10 ⁻⁴	1.251	1	1628.5

Table 8 – Solar panel array specifications.

Parameter	Value	Unit	Meaning
NMOT	42	°C	Nominal Module Operating Temperature (NMOT)
T _{aNMOT}	20	°C	Ambient T at NMOT
T _{STC}	25	°C	Cell T under STC
G _{NMOT}	800	W/m ²	Irradiance under NMOT
G _{STC}	1000	W/m ²	Irradiance under STC
I _{SCSTC}	13.45	A	Short circuit current under STC
V _{OCSTC}	49.4	V	Open circuit voltage under STC
β	0.27	%/°C	T coefficient of voltage
I _{mpSTC}	13.23	A	Maximum power point panel current under STC
V _{mpSTC}	41.2	V	Maximum power point panel voltage under STC
N _s	14	units	Assumed unit number of panels in series
N _p	23	units	Assumed unit number of panels in parallel

Another parameter has been iterated: the regulation setpoint, λ , in Equation (13). This parameter has been set to three different values for each configuration of daily demand and HDFV frequency, which are: 0, 88 and 176 kg. These scenarios represent the 0, 50 and 100% of H₂ storing capacity of T_{3,1}, T_{3,2}, T_{3,3}, T_{3,4} and T₄ combined at 25 °C and their maximum pressure conditions. The iteration of this parameter is with the aim of finding the importance of the amount of pressure of the aforementioned tanks in the HRS performance since this parameter affects the grid-connected mode scheduled production of H₂ of the electrolyzers. If the sum of the mass in those tanks is under the specified λ at the beginning of the day, more H₂ mass production is needed for the current day, above the daily demand prediction value. If the sum of the mass in those tanks is above the specified λ at the beginning of the day, less than the daily demand prediction value of H₂ production is needed in Equation (13).

Ensuring the daily demand of total LDFV and HDFV has been done by determining the initial mass of the vehicles at all arrivals. This is because it is assumed all vehicles, if possible, will be fully refuelled at 350 and 700 bar, respectively. Moreover, it is considered that the volume of the demand vehicles tanks is constant and known across all clients. For this reason, the initial mass of all vehicles that ensures the daily demand specified for each simulation scenario is computed.

In summary, 27 simulations have been determined, in which three scenarios of daily demand are iterated with three scenarios of HDFV intra-day frequency which are iterated with three scenarios of the regulation setpoint, λ .

For all simulation scenarios, the next profiles or parameters are the same:

- Hourly direct beam irradiance time series, G_b , from January 2016 in Zaragoza, Spain [50], shown as Supplementary Material.
- Hourly global irradiance profile, G_g , assumed equal to G_b .
- Time series of the hourly energy price, e_p , from January 2021 in Spain [51].
- Perfect daily prediction of the vectors of irradiance and energy price, \mathbf{p}_{e_p} and \mathbf{p}_{G_b} , is assumed, which means the day-ahead predictive algorithm takes perfect predictions of the next-day profiles.
- The simulation length is 31 days.
- The ambient temperature is considered constant at 298 K.

- The gasometer, and tanks T₂ to T₄ start at their maximum mass/pressure.
- MEGC initial condition is 0 kg.
- Solver ode23s with a maximum step time of 1s has been used.

In addition to the 27 simulations mentioned, one simulation of one year of operation has been performed.

5.3. Simulation results analysis and discussion

In this subsection, the main results of the multiple simulation scenarios are presented. First, a sample of the dynamic results of a specific simulation scenario is introduced to display the correct behaviour of the modelled HRS and the operational strategy.

Fig. 3 presents a detailed portion of the first day of simulation for λ set at 176 kg with a daily demand of 60 kg/day and 8 HDFV per day. It can be noted how the pressures of T₂, T₃ and T₄ have been controlled as desired in terms of order of priority in filling and emptying as well as how HDFV and LDFV have been completely refuelled. Two zoomed zones at the 20:00 h HDFV refuelling event and at the 21:00 h LDFV refuelling event are shown for T₃ and T₄. These zoomed sections show how the cascaded refuelling has been correctly simulated, since the different priorities of the tanks to service the FCEV until pressure equilibrium or refuelling completion is respected.

Simulation scenarios with λ set at 0, 88 and 176 kg are referred to as scenarios a), b) and c), respectively.

In Figs. 4 and 5 the HDFVs and LDFVs failed services are analysed, respectively. Here, it is shown all HDFV and LDFV services that have been left uncompleted for all simulation scenarios in terms of not-refuelled masses. The minimum and maximum not-refuelled masses per service are shown at the whiskers extremes. In each box, the lower and upper limits represent the 0.25 and 0.75 quantiles of the results, respectively, the median of the results is represented by the horizontal line inside the box, and “n” represents the number of FCEVs refuelling events uncompleted. Outliers are presented as circles and they are results with a value 1.5 times the interquartile range away from the box limits. For case a), the worst demand satisfaction with up to 181 HDFVs uncompleted services of a total of 248 services (8 HDFVs per day for 31 days of simulation) is shown. For case b), it is shown how the

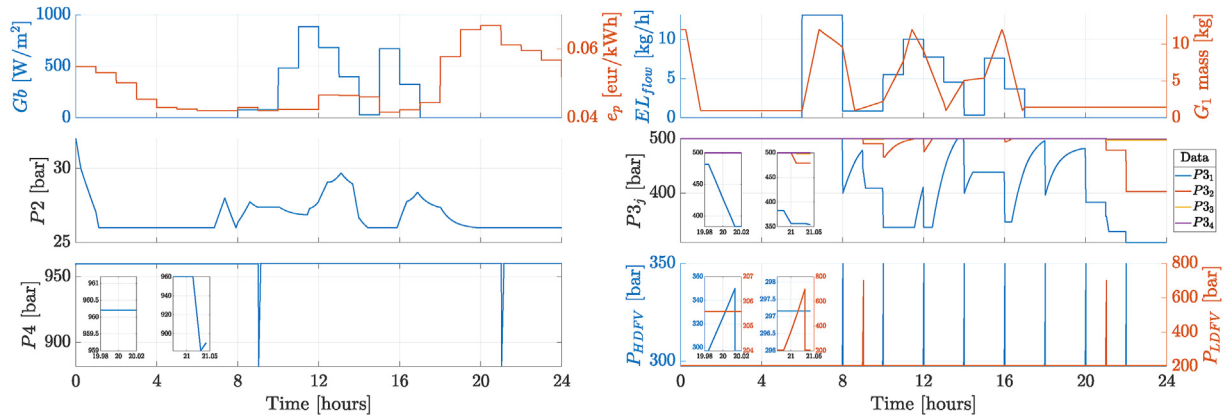


Fig. 3 – H₂ tanks pressure dynamic results for λ set at 176 kg with 60 kg/day and 8 HDFV per day. Results for the first day of January 2016.

increasing frequency of HDFVs or the daily demand has left more HDFV services unfulfilled with more than 15 kg of H₂ not refuelled off the 16.25 kg of demand (130 kg of HDFV daily demand for 8 HDFV per day).

In Fig. 5, similar results regarding the LDFV not-refuelled masses are shown. It is important to remember that for all scenarios the LDFV demand is 5 kg per service, hence we can appreciate many instances where LDFV service has not even been possible to start.

From Figs. 4 and 5, it can be seen how case c) has perfect demand satisfaction with 0 kg of H₂ mass not-refuelled for all daily demand and daily frequency of HDFV scenarios.

Fig. 6 gives an inside into how H₂ has been produced with energy from the grid as a result of the day-ahead predictive algorithm. As expected, the H₂ mass produced in grid-connected mode per day increases with the daily demand across a), b) and c). From such results, it can be deduced that

generally, more than 120 kg of H₂ must be produced with energy from the grid to achieve demand satisfaction.

Figs. 7 and 8 show the total mass serviced to HDFV and LDFV, respectively, for all simulation scenarios. There exists a numerical error of 1–2 kg in the final value due to rounding error and the solver tolerance. This error can be noted in Fig. 7: for 8 daily HDFV and 140 kg/day of case c) it should be expected 4030 kg of H₂ (130 kg/day in HDFV for 31 days) but results show 4032 kg.

Fig. 9 shows accumulated mass derived to MEGCs for all simulation scenarios. Case a) shows that the HRS has almost never been with all tanks full since the mass serviced to MEGCs is insignificant across 31 days of simulation per scenario. In case b), an important increase is shown in daily demand scenarios of 140 kg/day compared to the others. Moreover, case c) shows that a lot of mass-produced with the utility grid has been sold out to MEGCs, which maybe is not the optimal result in terms of emissions or cost.

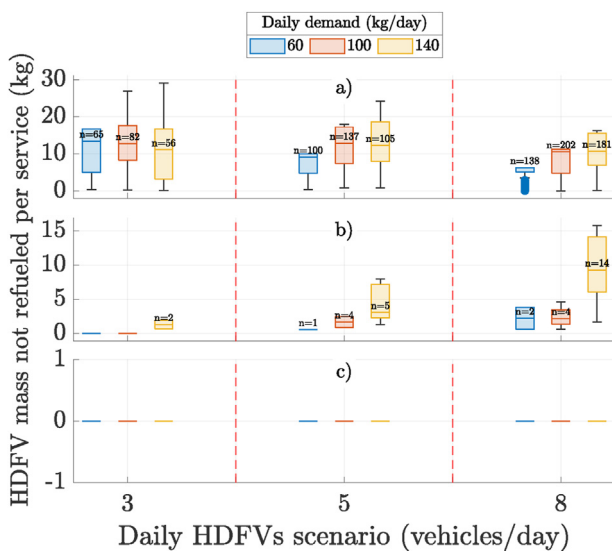


Fig. 4 – HDFV failed services results by daily demand, daily HDFV and regulation setpoint scenarios.

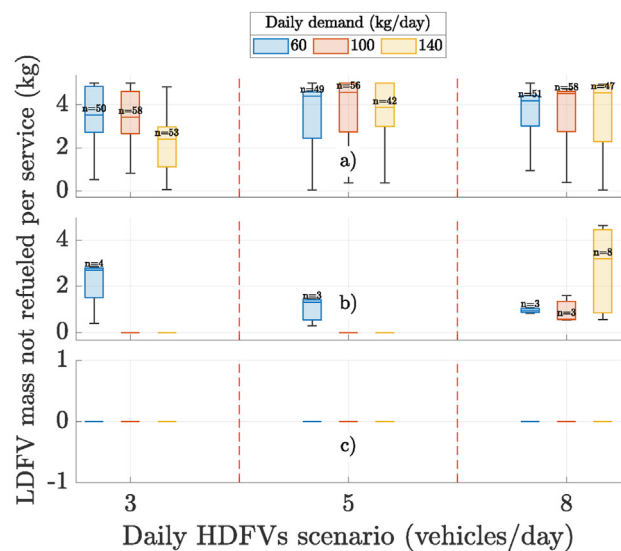


Fig. 5 – LDFV failed services results by daily demand, daily HDFV and regulation setpoint scenarios.

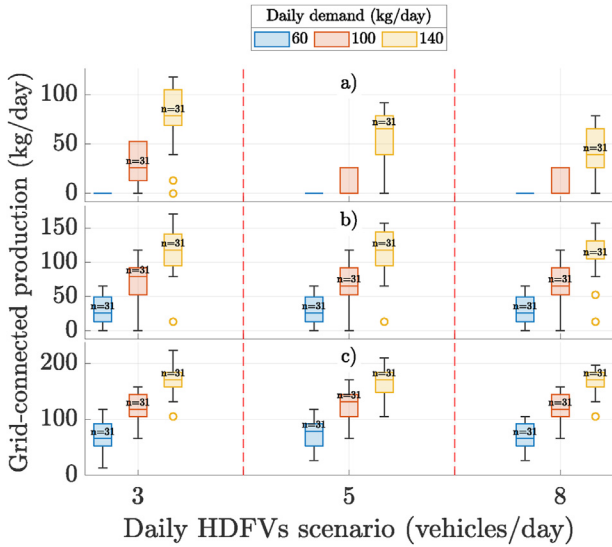


Fig. 6 – Grid-connected H₂ production per day of simulation.

For analyzing energy consumption, profit and emissions, only case c) has been considered since it is the only case where demand has been fulfilled. Fig. 10 shows the HRS accumulated energy consumption for case c). As expected, consumption increases with the HRS daily demand.

In Fig. 11, the HRS emissions due to utility grid consumption in Spain are shown. For this computation, the greenhouse gas emission intensity of the Spanish utility grid at 85 gCO₂eq/MJ has been considered [52] and a H₂ lower heating value of 119.9 MJ/kg [53]. From these results, an increase of 40 kg/day of H₂ demand has translated to 30 tCO₂eq emissions, approximately, at the end of the simulation. The same set of simulations have been performed for the month of July and the maximum value has been 56 tCO₂eq (scenario of 3 daily HDFV

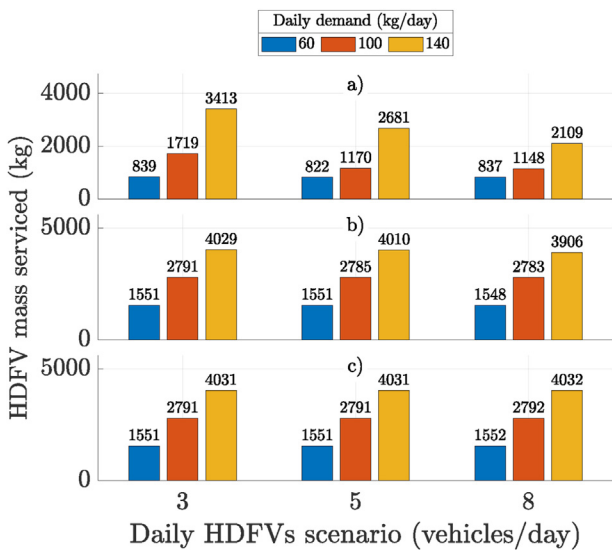


Fig. 7 – HDFV monthly H₂ mass refuelled.

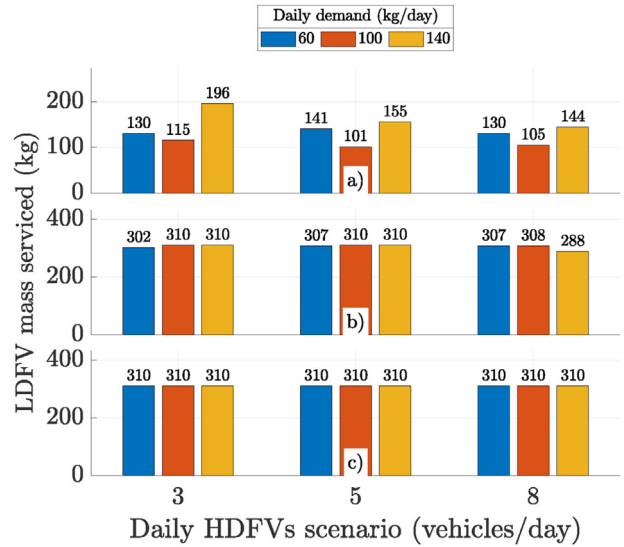


Fig. 8 – LDFV monthly H₂ mass refuelled.

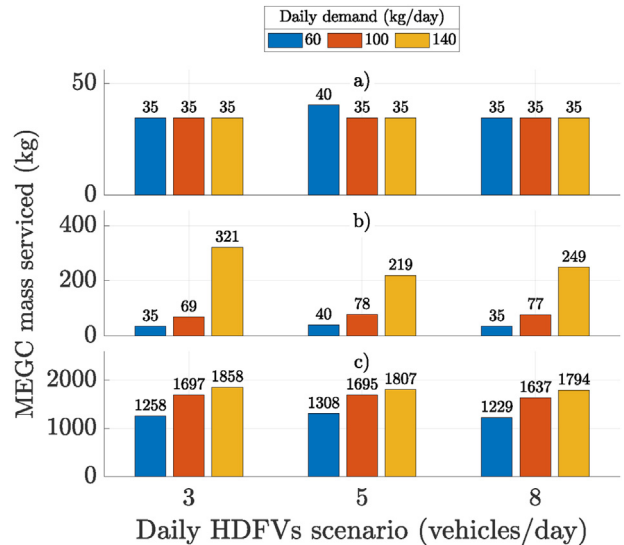


Fig. 9 – MEGC accumulated mass serviced.

with 140 kg/day), the best value has been –3 tCO₂eq (scenarios of 3 or 5 daily HDFV for 60 kg/day) which means the HRS has provided more energy to the grid than the energy consumed. Hence, a clear relation between demand, the time of the year and emissions is verified.

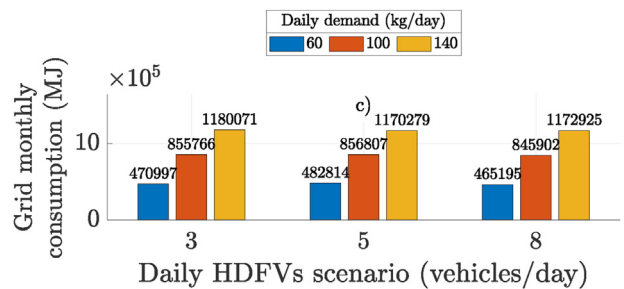


Fig. 10 – HRS monthly utility-grid energy consumption.

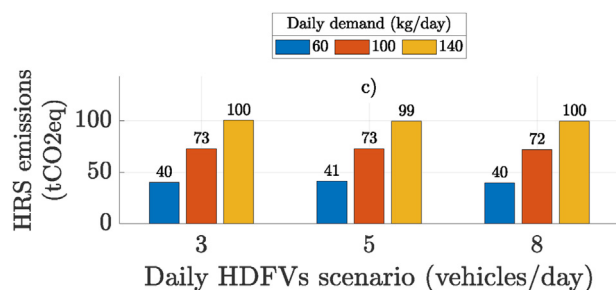


Fig. 11 – HRS monthly generated emissions.

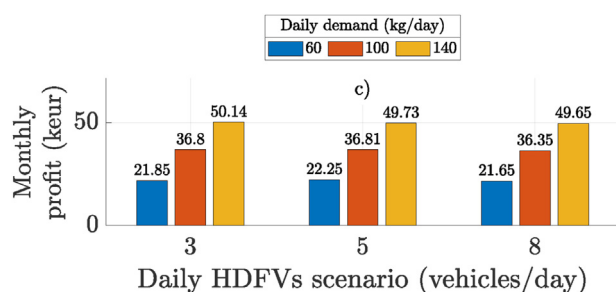


Fig. 12 – HRS monthly profits.

Fig. 12 presents the final profits of the HRS. From these results, only the utility grid consumption variable cost has been considered, energy injected into the utility grid has been assumed to be sold at the same cost value of the respective hour, and the H₂ selling price has been set at 8 €/kg.?

Concerning the one-year-long simulation, it has been configured with case c), 60 kg/day of H₂ demand and 8 HDFV/day. The figures showing the dynamics of pressure, power and emissions of this simulation are added as Supplementary Material to this paper. The total electrolysis production has been 34,615 kg of H₂. The emissions corresponding to the grid-connected mode H₂ production would account for 264.31 tCO₂eq in Spain. Nevertheless, the net HRS emissions considering all compressors consumption are reduced to 216.89 tCO₂eq due to the participation of the photovoltaic and battery systems in the HRS microgrid. The net utility grid consumption has been 708.81 MWh. These values result in a ratio of 6.26 kgCO₂eq/H₂kg and a greenhouse gas emission intensity of 52.26 gCO₂eq/H₂MJ when considering all electric loads, photovoltaic generation and the battery. This greenhouse gas emission intensity result is lower than that of fuels and biofuels in the transport sector, which is approximately 88 gCO₂eq/MJ [54]. Moreover, this result is reasonable considering the estimated 75 gCO₂eq/H₂MJ that on-site electrolysis H₂ production represented in the UK in 2020 [55].

6. Conclusions

To further develop, optimize and understand the capabilities of Hydrogen Refuelling Stations (HRSs), dynamic modelling tools must be used. In this paper, a generic HRS layout and

modelling approach is presented. This model has been parametrized according to a real HRS with on-site solar hydrogen electrolysis production, multiple compressors and compressed hydrogen tanks, an energy storage system, and three types of H₂ dispensing. HRSs are systems that, due to their complexity and operational constraints, cannot be simulated without an operational and control strategy. In this paper, an operational strategy formed by a finite-state machine and a day-ahead predictive algorithm are proposed to solve the HRS model operational problem. The model and operational strategy developed in this paper have provided satisfactory results through simulation. Results in terms of running costs, emissions and demand satisfaction are discussed based on a sensitivity analysis of H₂ demand and other parameters. In terms of minimizing emissions, the results show a trade-off between demand and the time of the year. Hence, if reducing emissions is an operational principle, hydrogen demand should be compromised during winter in Spain. Further research could be developed to optimize the sizing of the components or layout of the HRS, improving the operational strategy with an optimization-based solution, or improving the model to account for a better description of thermic dynamics in compression or dispensing.

Declaration of competing interest

The authors declare that they have no known competing financial interests or personal relationships that could have appeared to influence the work reported in this paper.

Acknowledgements

This research has been developed within the CSIC Interdisciplinary Thematic Platform (PTI+) Transición Energética Sostenible+ (PTI-TRANSENER+)[TRE2103000] as part of the CSIC program for the Spanish Recovery, Transformation and Resilience Plan funded by the Recovery and Resilience Facility of the European Union, established by the Regulation (EU) 2020/2094; project MASHED [TED2021-129927B-I00] funded by MCIN/AEI/10.13039/501100011033 and by the European Union NextGenerationEU/PRTR; and the project MAFALDA [PID2021-126001OB-C31] funded by MCIN/AEI/10.13039/501100011033 and by ERDF A way of making Europe.

Appendix A. Supplementary data

Supplementary data to this article can be found online at <https://doi.org/10.1016/j.ijhydene.2023.08.192>.

REFERENCES

- [1] Abdin Z, Zafaranloo A, Rafiee A, Mérida W, Lipiński W, Khalilpour KR. Hydrogen as an energy vector. *Renew Sustain Energy Rev* 2020;120(3). <https://doi.org/10.1016/j.rser.2019.109620>.

- [2] International Energy Agency (IEA). Global hydrogen review 2022. 2022. URL, www.iea.org/t&c/.
- [3] Net number of fcevs in europe | fchobservatory. URL, <https://www.fchobservatory.eu/observatory/technology-and-market/net-number-of-fcevs-annual>.
- [4] Stations map - h2stations.org. URL, <https://www.h2stations.org/stations-map/?lat=49.139384&lng=11.190114&zoom=2>.
- [5] Another record number of newly opened hydrogen refuelling stations in 2021 | TÜV SÜD. URL, <https://www.tuvsud.com/en/e-ssentials-newsletter/automotive-essentials/e-ssentials-01-2022/another-record-number-of-newly-opened-hydrogen-refuelling-stations-in-2021>.
- [6] HRS availability map. URL, <https://h2-map.eu/>.
- [7] Hoja de ruta del Hidrógeno. Una apuesta por el hidrógeno renovable, Ministerio para la Transición Ecológica y el Reto Demográfico 2020.
- [8] Another record number of newly opened hydrogen refuelling stations in 2021 | TÜV SÜD. URL, <https://www.tuvsud.com/en/e-ssentials-newsletter/automotive-essentials/e-ssentials-01-2022/another-record-number-of-newly-opened-hydrogen-refuelling-stations-in-2021>.
- [9] Another record addition of european hydrogen refuelling stations in 2022 | TÜV SÜD. URL, <https://www.tuvsud.com/en/press-and-media/2023/february/another-record-addition-of-european-hydrogen-refuelling-stations-in-2022>.
- [10] Genovese M, Fragiaco P. Hydrogen refueling station: overview of the technological status and research enhancement. 2023. <https://doi.org/10.1016/j.est.2023.106758>. 5.
- [11] Barhoumi EM, Okonkwo PC, Belgacem IB, Zghaibeh M, Tlili I. Optimal sizing of photovoltaic systems based green hydrogen refueling stations case study Oman. *Int J Hydrogen Energy* 2022;47:31964–73. <https://doi.org/10.1016/j.ijhydene.2022.07.140>.
- [12] Carr S, Zhang F, Liu F, Du Z, Maddy J. Optimal operation of a hydrogen refuelling station combined with wind power in the electricity market. *Int J Hydrogen Energy* 2016;41:21057–66. <https://doi.org/10.1016/j.ijhydene.2016.09.073>.
- [13] Okonkwo PC, Mansir IB, Barhoumi EM, Emori W, Radwan AB, Shakoor RA, Uzoma PC, Pugalanthi MR. Utilization of renewable hybrid energy for refueling station in Al-Kharj, Saudi Arabia. *Int J Hydrogen Energy* 2022;47:22273–84. <https://doi.org/10.1016/j.ijhydene.2022.05.040>.
- [14] Pang Y, Pan L, Zhang J, Chen J, Dong Y, Sun H. Integrated sizing and scheduling of an off-grid integrated energy system for an isolated renewable energy hydrogen refueling station. *Appl Energy* 2022;323. <https://doi.org/10.1016/j.apenergy.2022.119573>. 10.
- [15] Bartolucci L, Cordiner S, Mulone V, Pasquale S. Hydrogen based multi energy systems: assessment of the marginal utility of increasing hydrogen penetration on system performances. *Int J Hydrogen Energy* 2021;46(78):38588–602. <https://doi.org/10.1016/j.ijhydene.2021.09.108>.
- [16] Sprik S, Murphy D, Kuroki T, Terlip D, Eichman J, Penev M, Kurtz J. Hydrogen station capacity evaluation tool (hyscape). URL, <https://apps.openei.org/hyscape/#about>.
- [17] Mehrjerdi H. Off-grid solar powered charging station for electric and hydrogen vehicles including fuel cell and hydrogen storage. *Int J Hydrogen Energy* 2019;44:11574–83. <https://doi.org/10.1016/j.ijhydene.2019.03.158>.
- [18] Wang Y, Kazemi M, Nojavan S, Jermisittiparsert K. Robust design of off-grid solar-powered charging station for hydrogen and electric vehicles via robust optimization approach. *Int J Hydrogen Energy* 2020;45:18995–9006. <https://doi.org/10.1016/j.ijhydene.2020.05.098>.
- [19] Panah PG, Bornapour M, Hemmati R, Guerrero JM. Charging station stochastic programming for hydrogen/battery electric buses using multi-criteria crow search algorithm. *Renew Sustain Energy Rev* 2021;144. <https://doi.org/10.1016/j.rser.2021.111046>. 7.
- [20] Zhu L, He J, He L, Huang W, Wang Y, Liu Z. Optimal operation strategy of PV-charging-hydrogenation composite energy station considering demand response. *Energies* 2022;15:5915. <https://doi.org/10.3390/en15165915>.
- [21] Bahou S. Techno-economic assessment of a hydrogen refuelling station powered by an on-grid photovoltaic solar system: a case study in Morocco. *Int J Hydrogen Energy* 2023;48(61):23363–72. <https://doi.org/10.1016/j.ijhydene.2023.03.220>.
- [22] Genovese M, Blekhman D, Dray M, Fragiaco P. Hydrogen losses in fueling station operation. *J Clean Prod* 2020;248:119266. <https://doi.org/10.1016/j.jclepro.2019.119266>.
- [23] Genovese M, Blekhman D, Dray M, Fragiaco P. Hydrogen station in situ back-to-back fueling data for design and modeling. *J Clean Prod* 2021;329:129737. <https://doi.org/10.1016/j.jclepro.2021.129737>.
- [24] Genovese M, Blekhman D, Dray M, Fragiaco P. Multi-year energy performance data for an electrolysis-based hydrogen refueling station. *Int J Hydrogen Energy* 2023. <https://doi.org/10.1016/j.ijhydene.2023.04.084>.
- [25] Bhogilla SS, Niyas H. Design of a hydrogen compressor for hydrogen fueling stations. *Int J Hydrogen Energy* 2019;44:29329–37. <https://doi.org/10.1016/j.ijhydene.2019.02.171>.
- [26] Zhou H, Dong P, Zhu S, Li S, Zhao S, Wang Y. Design and theoretical analysis of a liquid piston hydrogen compressor. *J Energy Storage* 2021;41. <https://doi.org/10.1016/j.est.2021.102861>. 9.
- [27] Specklin M, Deligant M, Sapin P, Solis M, Wagner M, Markides CN, Bakir F. Numerical study of a liquid-piston compressor system for hydrogen applications. *Appl Therm Eng* 2022;216. <https://doi.org/10.1016/j.applthermaleng.2022.118946>. 11.
- [28] Ruffio E, Saury D, Petit D. Thermodynamic analysis of hydrogen tank filling. effects of heat losses and filling rate optimization. *Int J Hydrogen Energy* 2014;39:12701–14. <https://doi.org/10.1016/j.ijhydene.2014.06.069>.
- [29] Xiao J, Bénard P, Chahine R. Estimation of final hydrogen temperature from refueling parameters. *Int J Hydrogen Energy* 2017;42:7521–8. <https://doi.org/10.1016/j.ijhydene.2016.05.213>.
- [30] Talpacci E, Reuß M, Grube T, Cilibrizzi P, Gunnella R, Robinius M, Stolten D. Effect of cascade storage system topology on the cooling energy consumption in fueling stations for hydrogen vehicles. *Int J Hydrogen Energy* 2018;43:6256–65. <https://doi.org/10.1016/j.ijhydene.2018.02.030>.
- [31] Zhao L, Brouwer J. Dynamic operation and feasibility study of a self-sustainable hydrogen fueling station using renewable energy sources. *Int J Hydrogen Energy* 2015;40:3822–37. <https://doi.org/10.1016/j.ijhydene.2015.01.044>.
- [32] Bartolucci L, Cordiner S, Mulone V, Tatangelo C, Antonelli M, Romagnuolo S. Multi-hub hydrogen refueling station with on-site and centralized production. *Int J Hydrogen Energy* 2023. <https://doi.org/10.1016/j.ijhydene.2023.01.094>.
- [33] Deng Y, Miao N, Wu D, Liu Y, Zhai X, Tong J. A new high-pressure clearance seal with flexible laddered piston assembly in oil-free miniature compressor for potential hydrogen applications and investigation on its dynamic sealing efficiency. *Int J Hydrogen Energy* 2019;44:24856–66. <https://doi.org/10.1016/j.ijhydene.2019.07.245>.
- [34] Terlip D, Hartmann K, Martin J, Rivkin C. Adapted tube cleaning practices to reduce particulate contamination at

- hydrogen fueling stations. *Int J Hydrogen Energy* 2019;8692–8. <https://doi.org/10.1016/j.ijhydene.2018.06.190>.
- [35] Apostolou D, Xydis G. A literature review on hydrogen refuelling stations and infrastructure. current status and future prospects. 2019. <https://doi.org/10.1016/j.rser.2019.109292>. 10.
- [36] Xiao L, Chen J, Wu Y, Zhang W, Ye J, Shao S, Xie J. Effects of pressure levels in three-cascade storage system on the overall energy consumption in the hydrogen refueling station. *Int J Hydrogen Energy* 2021;46:31334–45. <https://doi.org/10.1016/j.ijhydene.2021.07.007>.
- [37] Rothuizen E, Mérida W, Rokni M, Wistoft-Ibsen M. Optimization of hydrogen vehicle refueling via dynamic simulation. *Int J Hydrogen Energy* 2013;38:4221–31. <https://doi.org/10.1016/j.ijhydene.2013.01.161>.
- [38] Heere D. *Modelling and optimization of a hydrogen refuelling station based on CH2P technology delivering decentralized hydrogen and electricity for mobility* by Daniel Heere. 2019.
- [39] Hirscher M. *Handbook of hydrogen storage*. Handbook of Hydrogen Storage: New Mate Future Energy Stor 2010. <https://doi.org/10.1002/9783527629800>. 03.
- [40] Makridis SS. Hydrogen storage and compression. In: Methane and hydrogen for energy storage. Institution of Engineering and Technology; 2016. p. 1–28. https://doi.org/10.1049/pbpo101e_ch1.
- [41] Rohatgi A. Webplotdigitizer: version 4.6. 2022. URL, <https://automeris.io/WebPlotDigitizer>.
- [42] Silla H. *Chemical process engineering: design and economics*. M. Dekker; 2003.
- [43] Li W. Simplified steady-state modeling for variable speed compressor, 50; 2013. p. 318–26. <https://doi.org/10.1016/j.applthermaleng.2012.08.041>.
- [44] Bhogilla SS, Niyas H. Design of a hydrogen compressor for hydrogen fueling stations. *Int J Hydrogen Energy* 2019;44:29329–37. <https://doi.org/10.1016/j.ijhydene.2019.02.171>.
- [45] Deshmukh SS, Boehm RF. Review of modeling details related to renewably powered hydrogen systems. *Renew Sustain Energy Rev* 2008;12:2301–30. <https://doi.org/10.1016/j.rser.2007.06.008>.
- [46] Fuentes M, Nofuentes G, Aguilera J, Talavera DL, Castro M. Application and validation of algebraic methods to predict the behaviour of crystalline silicon pv modules in mediterranean climates. *Sol Energy* 2007;81:1396–408. <https://doi.org/10.1016/j.solener.2006.12.008>.
- [47] Araujo G, Sánchez E. Analytical expressions for the determination of the maximum power point and the fill factor of a solar cell. *Sol Cell* 1982;5(4):377–86. [https://doi.org/10.1016/0379-6787\(82\)90008-4](https://doi.org/10.1016/0379-6787(82)90008-4).
- [48] Araújo N, Sousa F, Costa F. Equivalent models for photovoltaic cell – a review. *Revista de Engenharia Térmica* 2020;19:77. <https://doi.org/10.5380/reterm.v19i2.78625>.
- [49] Cardona P, Costa-Castelló R, Roda V, Carroquino J, Valiño L, Serra M. Model predictive control of an on-site green hydrogen production and refuelling station. *Int J Hydrogen Energy* 2023. <https://doi.org/10.1016/j.ijhydene.2023.01.191>.
- [50] Jrc photovoltaic geographical information system (pvgis) - european commission. URL, https://re.jrc.ec.europa.eu/pvg_tools/en/.
- [51] PVPC | esios electricidad. URL, <https://www.esios.ree.es/es/pvpc>.
- [52] Council of European Union. Draft - annexes on establishing a minimum threshold for greenhouse gas emissions savings of recycled carbon fuels and specifying a methodology for assessing greenhouse gas emissions savings from renewable liquid and gaseous transport fuels of non-biological origin and from recycled carbon fuels ref. Ares 2022:3836721. 20/05/2022 (2022). URL, https://ec.europa.eu/info/law/better-regulation/have-your-say/initiatives/12713-Renewable-energy-method-for-assessing-greenhouse-gas-emission-savings-for-certain-fuels_en.
- [53] Dincer I, Acar C. Review and evaluation of hydrogen production methods for better sustainability. *Int J Hydrogen Energy* 2014;40:11094–111. <https://doi.org/10.1016/j.ijhydene.2014.12.035>.
- [54] European Environment Agency. Greenhouse gas emission intensity of fuels and biofuels for road transport in europe (07/07/2023). URL, <https://www.eea.europa.eu/ims/greenhouse-gas-emission-intensity-of>.
- [55] Statista. Emissions of hydrogen fuel produced through onsite electrolysis in the United Kingdom in 2020, with a forecast for 2030 (06/07/2023). URL, <https://www.statista.com/statistics/1260557/uk-green-hydrogen-fuel-supply-chain-emissions/#statisticContainer>.

Acronyms

HRS: Hydrogen Refuelling Station
 FCEV: Fuel Cell Electric Vehicle
 HDFV: Heavy Duty Fuel cell Vehicle
 LDFV: Light Duty Fuel cell Vehicle
 MEGC: Multiple Element Gas Container
 T_i: Compressed H₂ gas tank number i
 C_i: H₂ compressor number i
 D_i: Dispenser number i
 SoC: State of Charge
 SOM: Simulation-Oriented Model
 ESS: Energy Storage System